FISEVIER

#### Contents lists available at ScienceDirect

# Acta Materialia

journal homepage: www.elsevier.com/locate/actamat



## Full length article

# Strain-induced multivariant martensitic transformations: A scale-independent simulation of interaction between localized shear bands and microstructure



S. Ehsan Esfahani<sup>a</sup>, Iman Ghamarian<sup>b</sup>, Valery I. Levitas<sup>a,c,d,\*</sup>

- <sup>a</sup> Department of Aerospace Engineering, Iowa State University, Ames, IA 50011, USA
- <sup>b</sup> Department of Materials Science and Engineering, University of Michigan, Ann Arbor, MI 48109, USA
- <sup>c</sup> Departments of Mechanical Engineering, Iowa State University, Ames, IA 50011, USA
- <sup>d</sup> Ames Laboratory, Division of Materials Science and Engineering, Ames, IA 50011, USA

#### ARTICLE INFO

#### Article history: Received 30 May 2020 Revised 30 June 2020 Accepted 30 June 2020 Available online 7 July 2020

Keywords:
Martensitic phase transformation
Polycrystal plasticity modeling
Strain softening
Shear bands
Contact problem

#### ABSTRACT

A scale-independent model for the interaction between multivariant phase transformations (PTs) and discrete shear bands is advanced and utilized to simulate plastic strain-induced PTs at high pressure. The model includes a scale-free phase-field theory for martensitic PTs. The localized shear bands are introduced via a contact problem formulation. That is, the continuous distribution of sliding displacements along the prescribed slip surfaces is modeled to reproduce the plastic-strain-induced stress concentrators necessary for nucleation of a high-pressure phase (HPP). The strain-induced PTs in the bi/polycrystalline samples subjected to compression and shear are studied. The simulations show a severe reduction in the PT pressure by the plastic shear in comparison to a hydrostatic condition, even below the phase equilibrium pressure, like in known experiments. Transformation kinetics versus shear strain for each martensitic variant and the volume fraction of the HPP in individual grains and the entire aggregate are determined. The stationary volume fraction of the HPP is the same for polycrystals consisting of 13 and 38 grains, and a further shearing does not cause PT. The local phase equilibrium condition based on the transformation-work criterion is satisfied at almost all stationary phase interfaces. A similar phase equilibrium condition in terms of stresses averaged over the entire polycrystal or HPP is fulfilled. These results are important for the development of the microscale kinetic equations and modeling the sample behavior in traditional and rotational diamond anvils during the high-pressure torsion, ball milling, friction, and other deformation-transformation processes.

© 2020 Acta Materialia Inc. Published by Elsevier Ltd. All rights reserved.

#### 1. Introduction

The interaction between PTs and plasticity considerably impacts mechanical properties [1]. Experimental studies in rotational ceramic/diamond anvils show that the superposition of large plastic shear and high pressure results in the production of new phases, which cannot be seen under hydrostatic conditions [2–8]. While many exciting phenomena, such as appearance of new phases and retaining of metastable phases at normal pressure, occur during shearing under high-pressure [3,4], a significant reduction in the PT pressure is the focus of the current study. As reported in [7,9–12], in comparison to the hydrostatic loading, the transformation pressure for various PTs (e.g., from hexagonal BN to super-

E-mail address: vlevitas@iastate.edu (V.I. Levitas).

hard wurtzitic BN [10], and from  $\alpha$  to  $\beta$  phase in Zr and its alloys [11–13]) can be reduced by a factor of 2 to 10 due to plastic deformations. A more dramatic reduction in the PT pressure, by two orders of magnitude, is observed for graphite to diamond PT in [14] due to an applied plastic shear.

The critical point to understanding this phenomenon is that there is a primary distinction between stress or pressure-induced PTs from one side and plastic strain-induced PTs under a high-pressure condition from the other side [3,4]. Pre-existing defects usually trigger the former. Since the number of these stress concentrators remains limited, the applied pressure must be increased significantly to activate nucleation sites with a lower potency (stress concentration). For plastic strain-induced PTs, nucleation of martensite or HPP occurs at the defects (shear-bands, shear-band and twin intersections, and dislocation pileups), generated in the course of the plastic straining.

<sup>\*</sup> Corresponding author at: Department of Aerospace Engineering, Iowa State University, Ames, IA 50011, USA.

The effective mechanism of reducing the PT pressure by plastic shear due to the concentration of all stress components at the tip of the dislocation pileups is justified analytically in [3,4]. The magnitude of all stress components is proportional to the number of dislocations in pileups, which can be increased substantially by increasing the plastic strain at a constant applied pressure. A more accurate and detailed description of the interaction between discrete dislocations and PT is presented in [15–17] by employing a nanoscale phase-field approach (PFA).

As a major difficulty in a traditional PFA, one needs to numerically resolve the interface widths and the dislocation core (which are around 1 nm). The mesh-independent solutions are numerically obtained by introducing at least 4–5 FEs across the interfaces. This requirement computationally restricts the PFA to sample sizes smaller than 1  $\mu m$ , which is significantly smaller than a realistic grain size (i.e.,  $10-1000 \ \mu m$  or even larger). To overcome this computational issue, some theories were developed [18] in which the interface width is artificially widened by three orders of magnitude (i.e., from 1 nm to 1  $\mu m$ ) while the interface energy remains the same. As a consequence, the stress/temperature hysteresis is proportionally reduced [19], and for the perfect crystals, barrierless nucleation starts near the phase equilibrium stress. The reduction in the stress hysteresis contrasts with the considerable pressure and stress hysteresis in the experiments for many PTs, especially at high pressures. As an example, for a graphite-diamond PT at zero temperature and hydrostatic pressure [14], the equilibrium pressure (2.45 GPa) is approximately two orders of magnitude smaller than the lattice instability and the PT pressure (250 GPa) for an ideal graphite crystal. In quasi-hydrostatic experiments, the pressure required to transform a real (defective) graphite crystal to diamond, 70 GPa, is also much higher than the phase equilibrium pressure.

A microscale PFA approach to study the martensitic PT was initially proposed in [20,21] and advanced in [19]. This model has been applied to reproduce discrete martensitic microstructures in samples greater than 100 nm with no upper limits. In this study, the volume fraction of the martensite, c, is the order parameter which is responsible for the material instability due to strain softening. This instability leads to the transformation strain localization, and consequently a discrete martensitic microstructure. This is opposed to the traditional micromechanical or phenomenological models [22,23], in which a smeared distribution of martensite is obtained due to the lack of material instabilities. The volume fractions of martensitic variants are just internal variables and not the order parameters, i.e., no interfaces between martensitic variants are reproduced. One can expect a highly mesh-dependent solution as a result of dropping the gradient term to make the model scale-independent. However, as examined in [19], this scale-free model is practically mesh-independent since unstable regions are limited to narrow interfaces between phases with the width of a single FE. We utilize this approach to describe the transformational part of our model, which is developed to examine the interaction between the PT and discrete dislocations. A summary of formulations for this part of the model can be found in the supplemental material [24].

Concerning the PFA to perfect dislocations, upscaling [25,26] is done by increasing the dislocation height while the Burgers vector is fixed. This assumption, however, decreases the stress concentration and the transformation shear proportionally. The coupling between discrete dislocations and martensitic transformations was described within a nanoscale PFA [15–17,27,28] in a nano-sized bicrystal.

In this paper, we elaborate on a scale-free model for the interaction between PT and localized plasticity, which has been introduced recently in [29], and implement it for several detailed simulations of the relevant model problems. The key innovation of

this model is a scale-free replication of the dislocation pileup-like stress concentrators as the main mechanism for the nucleation and evolution of the plastic-strain-induced martensitic phase. To this end, we propose a contact problem formulation to simulate generation and continuous evolution of multiple dislocations in pileups along the prescribed slip surfaces, in combination with the scale-free PFA from [19-21]. The same formalism is applied if instead of dislocation pileups [30] one treats thin twines [31], shear bands [32], or shear cracks [33]. ABAQUS FE code is used to implement our model through the user subroutines for defining material and frictional behaviors [34]. It is demonstrated that although the model presented herein is much simpler than the nanoscale PFA models in [15-17,27,28], it is fully able to reproduce the stress field of a single dislocation and the microstructure evolution of HPP at evolving dislocations in a bicrystal sample subjected to compression and shear. The model does not possess a characteristic size that should be resolved with several finite elements, and is consequently scale-free, and can be implemented to a sample size from tens of nm to km, e.g., for geophysical applications. For geometrically similar bicrystal samples, the model produces similar stress fields, evolution and stationary state of the HPP morphology, and the relative sliding (i.e., number of dislocations within each slip system) proportional to the sample size. For the nanoscale bicrystal, our much simpler scale-free model produces very similar results to the single-variant nanoscale PFA in [15–17]. After showing the efficiency of the new model, we solve problems on the interaction between two-variant PT and localized plasticity in a polycrystalline aggregate under compression and shear. The shape and orientation of the grains were generated by utilizing DREAM.3D [35] and MTEX [36]. This work illuminates how localized plastic deformation drastically reduces the PT pressure in known experiments [7,9–14]. Our preliminary results with a simplified version of the model and a polycrystalline aggregate with 3 times smaller number of grains are published in [29].

Here, vectors and tensors are designated with boldface letter;  $\mathbf{A} \cdot \mathbf{B}$  and  $\mathbf{A} : \mathbf{B}$  represent the contraction and double contractions of two tensors, respectively; subscript s designates the symmetric part of the tensor;  $\tilde{A}$  stands for the average of A over the grain; and  $\tilde{A}$  defines the average of A over the whole sample. All grain orientations are specified in the Bunge-Euler convention [37], and crystals are initially defect-free. Moreover, two Bunge angles  $\varphi=135^\circ$  and  $\varphi_2=0^\circ$  are constant in this study, and  $\varphi_1$  (describing rotation about the out-of-plane normal) varies for each grain and are identified for each example.

### 2. Dislocations via contact problem

According to the definition expressed in [30,31], a dislocation is produced by a relative sliding of two sides of a cut (slip plane) in an elastic continuum, by a Burgers vector **b**, while the normal components of the displacement and the traction across the cut remain continuous. Along the same line, one can define multiple continuously distributed dislocations by the relative sliding  $u_s$ along the same slip surface. Similar continuity conditions for the normal components of the displacement and the traction across the contact surface are applied for the relative sliding in a contact problem between the two deformable bodies [34,38]. This was the reason for us [29] to propose a model with a continuous distribution of dislocations by solving the contact problem. Previously, the contact problem was used in [39,40] to model dislocations along the fixed or moving semicoherent phase interface. A similar procedure, but for single dislocation, called "cut-displace-glue" was recently analyzed in [41].

While in [29], the simplest sliding rules were given, here we present a more general formulation. Within a slip plane i, the sliding  $u_{ij}^{s}$  occurs along the specific slip directions ji determined by

crystallography, and the sliding rate is determined by Schmid's law and the flow rule:

$$\dot{u}_{ij}^s = \begin{cases} 0 & \text{if} & |\tau_{ij}| \le \tau_{ij}^c(u_{ij}^s, \sigma_n^i) \\ q_{ij}(|\tau_{ij}|, u_{ij}^s, \sigma_n^i) \text{sign}(\tau_{ij}) & \text{if} & |\tau_{ij}| > \tau_{ij}^c(u_{ij}^s, \sigma_n^i), \end{cases}$$
(1)

where  $\tau_{ij}$  is the resolved shear stress,  $\tau^c_{ij}$  is the athermal resistance to sliding,  $\sigma^i_n$  is the normal stress at the *i*th slip plane, and  $q_{ij}$  is a function determined from experiments. Sliding displacements  $u^s_{kl}$  for the other slip systems can be also arguments in functions in Eq. (1).

Continuity of the normal displacements and traction is expressed as

$$u_i^{n1} = u_i^{n2}; \qquad \sigma_{n1}^i = \sigma_{n2}^i; \qquad \tau_1^i = \tau_2^i,$$
 (2)

where  $\tau^i$  is the shear stress vector at the *i*th slip plane. When the effect of viscosity is neglected, Eq. (1) is substituted with its rate-independent counterpart:

$$\dot{u}_{ij}^{s} = \begin{cases}
0 & \text{if } |\tau_{ij}| < \tau_{ij}^{c}(u_{ij}^{s}, \sigma_{n}^{i}) \text{ or } |\tau_{ij}| = \tau_{ij}^{c}(u_{ij}^{s}, \sigma_{n}^{i}) \\
& \text{and } sign(\tau_{ij})\dot{\tau}_{ij} \leq \dot{\tau}_{ij}^{c}(u_{ij}^{s}, \sigma_{n}^{i}); \\
& |\dot{u}_{ij}^{s}|sign(\tau_{ij}) \neq 0 \text{ if } |\tau_{ij}| = \tau_{ij}^{c}(u_{ij}^{s}, \sigma_{n}^{i}) \\
& \text{and } sign(\tau_{ij})\dot{\tau}_{ij} = \dot{\tau}_{ij}^{c}(u_{ij}^{s}, \sigma_{n}^{i}),
\end{cases}$$
(3)

where  $|\dot{u}^{\rm s}|$  is determined from the consistency condition  $sign(\tau_{ij})\dot{\tau}_{ij}=\dot{\tau}^c_{ij}(u^s_{ij},\sigma^i_n)$ . The rate-independent formulation assumes that the shear stress relaxation to  $\tau_c$  happens instantly and the kinetics of dislocation motion is very fast until the equilibrium configuration is reached. In combination with finite-rate PT kinetics, this means that the motion of dislocation and plastic relaxation processes are much faster than PT. Equation  $|\tau_{ij}|=\tau^c_{ij}(u^s_{ij},\sigma^i_n)$  resembles the local equilibrium equation between the resolved shear stresses and athermal resistance to slip for continuously distributed dislocations [30,31].

When we neglect the dependence of  $\tau^c_{ij}$  on  $u^s_{ij}$  and  $\sigma^i_n$ , i.e., for constant  $\tau^c_{ij}$ , Eq. (3) reduces to

$$\dot{u}_{ij}^{s} = \begin{cases} 0 & \text{if } |\tau_{ij}| < \tau_{ij}^{c} \text{ or } |\tau_{ij}| = \tau_{ij}^{c} \text{ and } sign(\tau_{ij})\dot{\tau}_{ij} < 0; \\ |\dot{u}_{ij}^{s}|sign(\tau_{ij}) \neq 0 & \text{if } |\tau_{ij}| = \tau_{ij}^{c} \text{ and } \dot{\tau}_{ij} = 0. \end{cases}$$
(4)

Finally, for the current 2D applications, for which there is only one slip direction for each slip plane, we simplify Eq. (4) to

$$\dot{u}_i^s = \begin{cases} 0 & \text{if } |\tau_i| < \tau_i^c \text{ or } |\tau_i| = \tau_i^c \text{ and } sign(\tau_i)\dot{\tau}_i < 0; \\ |\dot{u}_i^s| sign(\tau_i) \neq 0 & \text{if } |\tau_i| = \tau_i^c \text{ and } \dot{\tau}_i = 0. \end{cases}$$

$$(5)$$

For multiphase materials, the critical resolved shear stress  $\tau^c_{ij}$  depends on phases, and if a certain portion of the slip plane is located along the phase interface, the smallest  $\tau^c_{ij}$  is used.

A similar presentation is valid for thin twins along the twinning plane i with shear direction j, which can be modeled by the motion of partial (twinning) dislocations [31]. The number of dislocations (complete or partial) along each slip direction is determined by  $n_{ij} = |u_{ij}^s|/|\boldsymbol{b}_{ij}|$ . Since shear cracks can also be presented as dislocation pileups [33], they can be included in our formulation as well. Similar, macroscopic shear bands, which may not coincide with crystallographic slip planes and directions [32], are also included in the current formalism.

The only difference between all these mechanisms is in the specific sliding rules in Eq. (1), while the continuity conditions Eq. (2) apply to all of them. Since the evolution of the continuously distributed dislocations or localized shears along discrete slip surfaces is now formulated as the contact problem in continuum mechanics, well-developed FEM algorithms and codes [34,38] for the solution of contact problems are available.

The Burgers vector or, more generally, sliding displacement  $u_{ij}^s$  is the only spatial scale parameter in the contact problem. In contrast to the nanoscale PFA to dislocations [15–17,42], for which characteristic length should be resolved with 4–6 integration points, displacement  $u_{ij}^s$  should not be resolved and can be significantly smaller than the size of a single element. Thus, this model is scale-independent and therefore can be used for arbitrary large samples. Our scale-free PFA for multivariant martensitic PTs [19–21] is presented in the supplementary material [24].

#### 3. Numerical results and discussion

The simplest formulation of the model is utilized in the simulations. The phase transformations between body-centered cubic (bcc) low-pressure phase (LPP) and body-centered tetragonal (bct) high-pressure phase (HPP) along with dislocation slip are studied. Since temperature does not change during shearing in rotational diamond anvils due to small sample thickness and high thermal conductivity of diamonds, isothermal processes at room temperature are considered.

A complete system of equations and material parameters are presented in the supplemental material. Similar to all previous studies on this topic [3,4,15-17,29], we consider a generic model material. To work with a specific material, significant coupled highpressure-shear and microstructural experiments with the multiscale theory should be performed for parameter identification, see [8]. That is why we use the simplest model, in particular with small elastic strain and linear elasticity. The most important material parameters are as follows: the thermal energy difference between HPP and LPP  $\Delta G^{\theta} = 1.0$  GPa ( $\theta$  is the temperature); the phase equilibrium pressure between HPP and LPP  $p_e = 10$  GPa; the lattice instability pressure for the LPP  $p_{cr} = 20$  GPa, and the transformation strains are  $\varepsilon_{tx} = \varepsilon_{ty} = -0.05$  and  $\varepsilon_{txy} = 0.2$ . We assume that the critical resolved shear stress,  $\tau_c = 1.0$  GPa for the bicrystal problems and  $\tau_c = 0.3$  GPa for a polycrystal, is the same for all slip systems for the LPP and both martensitic variants of the HPP.

A complete numerical simulation should consider a 3-D polycrystalline aggregate with a minimum of a thousand grains which have various orientations with respect to the sample frame. The body centered-cubic lattice includes more than 12 equivalent slip systems, each should be introduced in the simulation by a distinct contact surface. However, involving the contact and the strainsoftening dramatically increases nonlinearities of the formulation, which leads to numerical convergence issues and very long simulation time. That is why, similar to [29], we consider multiple 2-D examples for bicrystal and a polycrystalline aggregate and a limited number of active slip systems as the best compromise between computationally cost-effective formulation and a physical adequate one.

The model is implemented in FE code ABAQUS [34] using user material (UMAT) subroutine. The shear crack definition in ABAQUS gives us the capability to introduce contact pairs in the middle of our samples and in many regions without defining several parts in contact. ABAQUS FRIC subroutine allows us to implement the chosen contact friction formulation. Also, the proper mesh, the grain structures and orientations, and the corresponding slip systems are produced by MTEX [36] and DREAM.3D [35]. Quadratic plane strain elements are utilized in order to improve the convergence for straight edge dislocations that we have considered for several problems. Finding active slip systems is a hotly debated topic in the plastic deformation of bcc crystals. {110} < 111 > is the most preferred deformation mode; however, sliding along other slip systems,  $\{112\}$  < 111 > and  $\{123\}$  < 111 > are also observed [43]. The transmission electron microscopy investigations revealed that plastic deformation mainly occurs along {110} < 111 > and {112} < 111 > slip systems [44]. Considering the plane strain con-

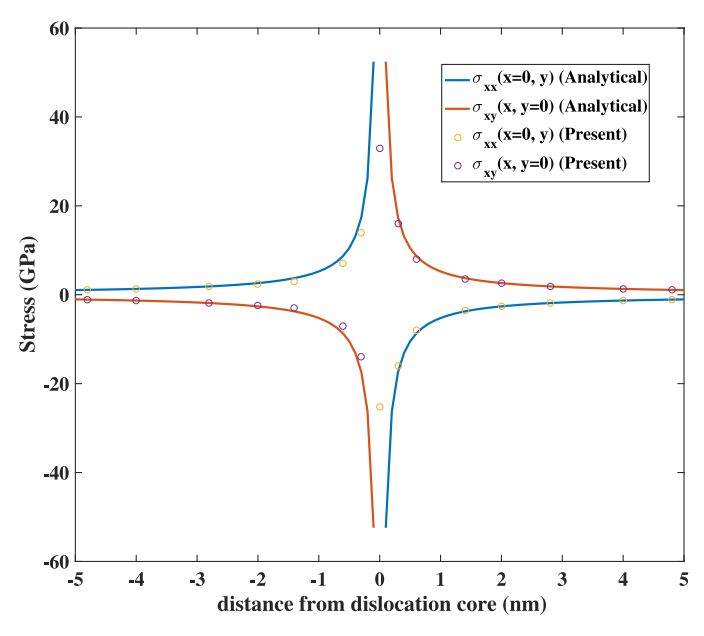


**Fig. 1.** A comparison of the stress fields near a dislocation obtained in our FE simulation and the analytical solution from [30].

ditions implemented in this study,  $\{112\}$  < 111 > slip systems must be selected, which are assumed to be inherited by the bct crystal during PT.

Stress fields near a single dislocation. A single dislocation is introduced by prescribing homogeneous sliding displacement  $u_s = |u_s| = |b|$  along a contact line in a half of a relatively large sample. Linear quadrilateral elements with the mesh size of 0.3b are utilized. Numerical results for shear and normal stresses are in a good agreement with the analytical solution [30] (see Fig. 1) for a distance larger than 0.3b from the dislocation position, which is well within the dislocation core. This consistency confirms the feasibility of representing dislocations by the contact definition as a practical approach.

# 3.1. Strain-induced phase transformation in a bicrystal

Sample. To begin with, we solve a problem on PT induced by the dislocation pileup in a bicrystal, similar to that in [15], where an advanced nanoscale PFA was applied to study the evolution of both HPP and dislocations. Respecting the same conditions as in [15] for the sake of comparison, we consider a sample with the size of  $50 \times 30$  which consists of (see Fig. 2): (a) two rectangular grains with the size of  $h \times L = 25 \times 20$  each, in which PT and/or the sliding problem (to imitate the dislocation pileup on the grain boundary) are solved; here h and L are the height and widths of the grains; (b) two rectangles above and below the bicrystal having the size of  $50 \times 5$ , which are simulating the elastic accommodation of the surrounding grains. In these two regions, only the elastic problem is studied.

Two types of loading are considered.

- Type-1: the PT is allowed in the right grain after reaching the stationary state for the dislocation solution in the left grain.
- Type-2: PT and dislocations are evolving simultaneously from the beginning of applying the shear strain.

Pressure-induced nucleation at a single dislocation. A single dislocation as a nucleation site was introduced at the center of the sample by producing uniform shear along the contact surface. A homogeneous normal stress was applied along all the external surfaces reproducing the hydrostatic loading of a crystal. The minimum hydrostatic pressure for nucleation of the HPP is  $p_h=14.70$ 

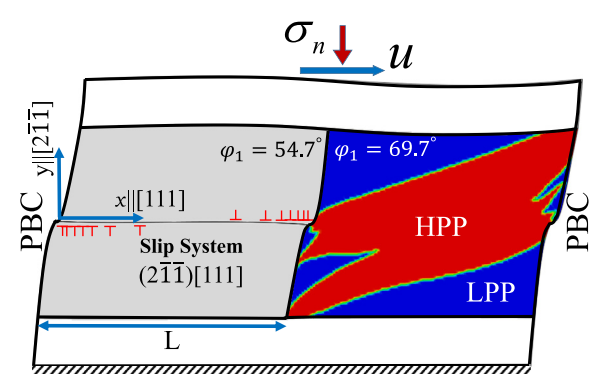


**Fig. 2.** The stationary solution for a bicrystal under compression and shear at  $\gamma=0.2$ . The interaction between the dislocation pileup and the grain boundary in the left grain leads to the phase transformation from LPP (blue) to HPP (red) in the right grain. (For interpretation of the references to color in this figure legend, the reader is referred to the web version of this article.)

GPa. This nucleation pressure is not far from  $p_h = 15.75$  GPa reported in [15] by utilizing a nanoscale PFA.

Bicrystal under compression and shear. In Fig. 2, the top side of the bicrystal system is under a constant uniformly distributed Cauchy (true) stress  $\sigma_n$  and a homogeneous horizontal displacement, u, expressed by macroscopic shear strain  $\gamma = u/h$ . Periodic boundary conditions for displacements are implemented at the lateral sides, and a zero displacement is applied at the bottom side. Initially, the both grains are completely in LPP, and we study the PT without plasticity in the right grain, and plasticity without PT in the left grain, along a horizontal contact line as an active slip system. For analysis of the PT, the 2D version of pressure,  $p = -0.5(\sigma_x + \sigma_y)$ , is used, since for  $\varepsilon_{tz} = \varepsilon_{ty}$  and plane strain conditions, it contributes to the transformation work. Before applying the shear, the vertical stress  $\sigma_n = 3.05$  GPa is applied which produces an averaged pressure of 2.0 GPa in each grain. The loading type-1 is considered. At constant  $\sigma_n$ , during a gradual application of the shear strain  $\gamma$  to the top edge, the contact surfaces start slipping when the shear stress along the slip direction reaches  $\tau_c$ . This leads to relative displacements of upper and lower sides of the contact surface, which produce pairs of dislocations with different signs. With increasing  $\gamma$ , more pairs of dislocations nucleate. The motion of these dislocations to the grain boundaries produces a pileup at the middle of the grain boundary, and steps from both sides of the sample. For  $\gamma = 0.2$ , the stationary state with the relative displacement corresponding to  $7|\mathbf{b}|$  appears, which indicates a pileup with the same number of dislocations as reported in [15].

For the sake of comparison, the results for the same bicrystal and loading in [15] are exhibited in Fig. 3(a) and (b). In Fig. 4(a), the evolution of martensite microstructure in the right grain is presented. Because of the high stress concentrations at the tip of dislocation pileups, two HPP regions are nucleating and growing. Since two pileups are quite close to each other, these HPP plates start interacting which results in a coalescence and a morphological transition with the final averaged concentration of the HPP  $\tilde{c}=0.58$  (versus  $\tilde{c}=0.51$  in [15]). Moreover, a close similarity between the HPP morphology achieved by the current method and the one in [15] (see Fig. 3(a) and (b)) is evident. This resemblance proves that the current scale-independent model is effectively able to simulate the results by a far more sophisticated PFA, which is computationally restricted to nanoscale samples.

It should be noted that experimentally, the averaged pressure and shear over the sample are measured after the completion of PT. Therefore, at the stationary state of the PT and due to a volume reduction in the right grain, the pressure averaged over both grains is dropped to  $\bar{p}=0.07$  GPa, i.e., more than 100 times lower

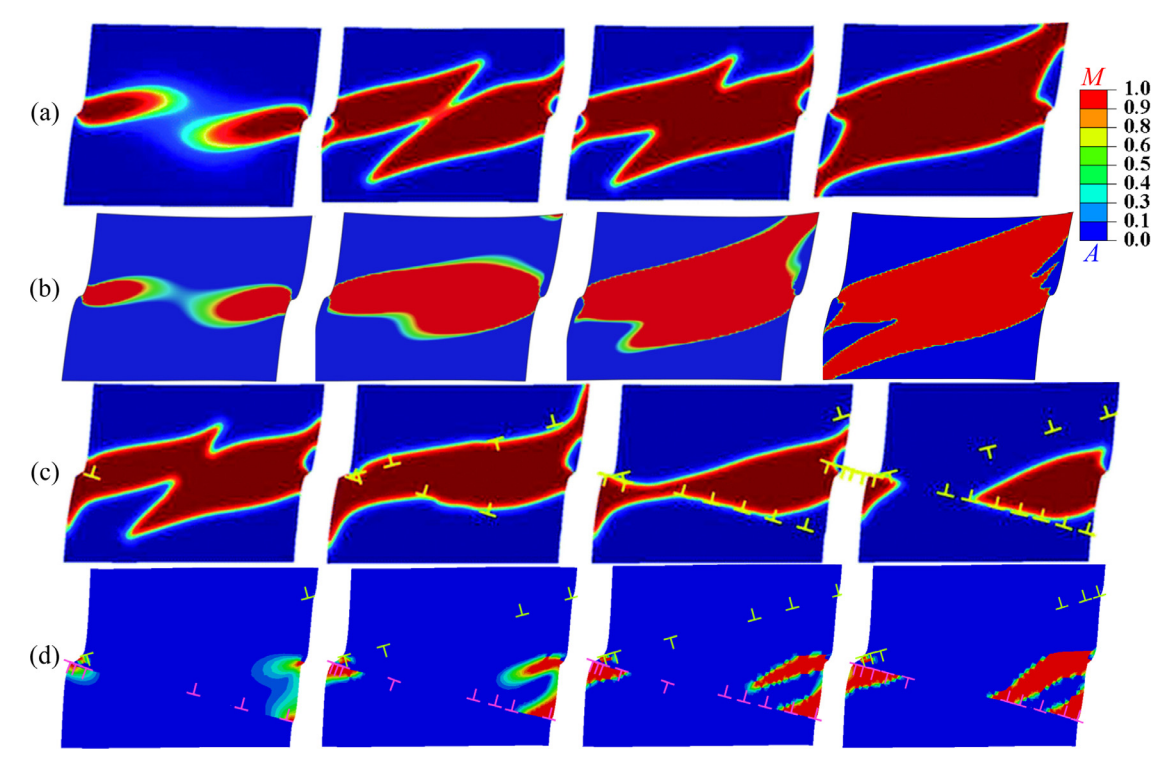


**Fig. 3.** Comparisons between the evolution of the HPP and dislocations in the right grain for the results reported in [15] (rows a and c), and the results presented in this study (rows b and d). The applied shear strain  $\gamma = 0.2$ , loading type-1, and  $\varphi_1 = 69.7^{\circ}$ . In (a) and (b) solutions are without dislocations in the right grain, and in (c) and (d) with dislocations.

than  $p_h = 14.7$  GPa for the hydrostatic conditions. Thus, our model describes the severe PT pressure reduction due to a plastic shear in the experimental results, by one order of magnitude in [7,9–12] and even two orders of magnitude for PT from graphite to cubic diamond [14]. Note that PT pressure under shear is also significantly below the phase equilibrium pressure under hydrostatic conditions, 10 GPa, like in some experiments [7,13].

In Fig. 3(c) and (d), the dislocation activities are involved in the right grain by introducing two slip systems with  $\pm$  15° to the x axis, to replicate the geometry presented by [15]. Also, we allow the PT and sliding in the right grain just after dislocations reach a stationary configuration in the left grain. Due to instantaneous dislocation kinetics Eq. (4), dislocation evolution and stress relaxation are significantly faster than the PT, i.e., the PT are suppressed. This is the main reason for the difference in HPP evolutions in Fig. 3(c) [15] and the current result in Fig. 3(d). Instead of two nuclei in Fig. 3(d) at the tips of the dislocation pileup in the adjoining grains, only one nucleation is observed. However, two other nuclei appeared in the regions with extra atomic planes and high compressive stresses at dislocation pileups in the same grains. The transformed regions do not pass the slip planes due to the athermal resistance to the interface motion, which is produced by the tensile stresses caused by missing atomic planes. In total, the HPP is much smaller than one in Fig. 2(a). Still, like in the nanoscale PFA [15,16], it is possible to produce such pressure-shear loadings that PT takes over the dislocation plasticity. The results essentially depend on the orientation of grains.

Fig. 4( b) presents a loading scenario for which PT and dislocations are included from the beginning of applying the shear (loading type-2). The prescribed shear,  $\gamma$ , applied normal stress,  $\sigma_n$ , at the top, and all the boundary conditions are the same as in the above example. The different morphology for this loading condition can be understood by making a comparison of the stress field near the dislocation pileup for both cases (see Figs. 6 and 7). It is evident that the stress concentration at the pileup is initially

smaller than the corresponding values for the loading type-1. In Fig. 7, the evolutions of pressure and shear for the right grain are presented by isolines for the loading type-2. Because dislocations in the left grain are not in their stationary states yet, the stress concentrators at the pile up are less effective than for the loading type-1 scenario. However, when both dislocations in the left grain, and HPP in the right grain reach their stationary states, the stress field is approximately similar to the one presented in Fig. 6. As a result, for the loading type-2, the HPP concentration ( $\tilde{c} = 0.56$ ), and the pressure averaged over the both grains ( $\bar{p} = 0.1$  GPa) are insignificantly different from those for the loading type-1.

To illustrate the effect of changing the sample size on the martensitic microstructure and the number of dislocations, in Fig. 5, we consider one, two, and three orders of magnitude larger samples in length and height with the same boundary and loading conditions as explained in Fig. 2, as well as the same Burgers vector. The microstructure evolution of HPP for all of these samples is exactly the same; in Fig. 5, one of them is demonstrated as a representative of all the cases. As a result of the same stationary solution for the HPP, the average pressure, shear, volume fraction of martensite, and transformation work are the same. As one may see in the Fig. 5, the maximum number of dislocations, and the scale factor are in a proportional relationship. This can be interpreted as the only reason that the same morphology of the HPP is produced. Also, in Fig. 5, the distribution profiles of the dislocations along the slip plane are exactly the same at the stationary state for all the sample sizes. All these results confirm that our model is scale-independent.

A change in the orientation of the right grain is not changing the stationary dislocation configuration in the left grain; however, from a comparison between Fig. 4(a) and (c) (both subjected to the loading type-1), a profound effect of the grain orientation on the HPP morphology is visible. In Fig. 4(d), we include the plasticity with the PT in the right grain ( $\varphi_1 = 89.7^{\circ}$ ) by predefining two slip systems with a  $\pm$  35.26° angle with respect to the *x* axis (the

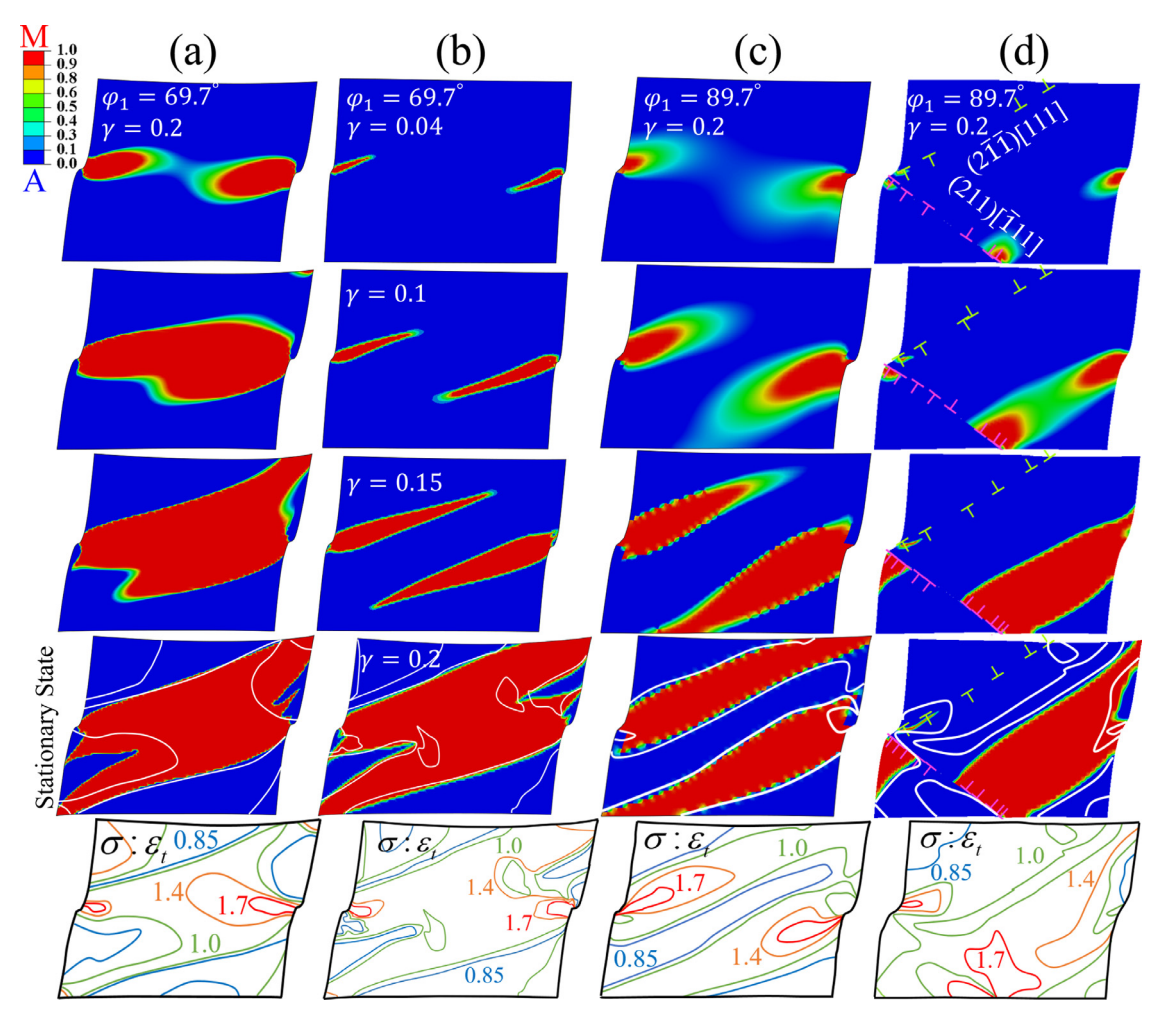
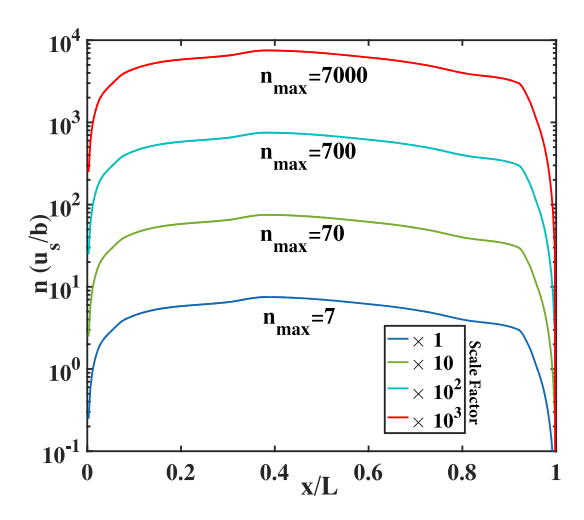


Fig. 4. (a): HPP nucleation and evolution for  $\varphi_1=69.7^\circ$  and loading type-1. (b): HPP nucleation and evolution for  $\varphi_1=69.7^\circ$  and loading type-2. (c): HPP nucleation and evolution for  $\varphi_1=89.7^\circ$  and loading type-1. (d): Concurrent nucleation and evolution of the dislocations and HPP for  $\varphi_1=89.7^\circ$  and loading type-1. Bottom row: transformation work contour lines. White isolines for stationary solutions represent the equilibrium transformation work,  $\sigma: \varepsilon_t = \Delta G^\theta(\theta) = 1.0$  GPa. Since they are very close to the most of interfaces, the local phase interface thermodynamic equilibrium condition is met.

coordinate system is defined in Fig. 2). Due to a rate-independent kinetics for dislocations in Eq. (4), they nucleate and grow faster than PT in this case, and the stress relaxation is more related to dislocation motions than to the PT. HPP nuclei appear initially at the pileups, and two of them coalesce. There is a small region of HPP in the left side of the right grain which is due to the dislocation pileup which resulted from the appearance of the dislocations near a small region. Since the nucleation of the dislocations introduces an athermal friction for the HPP evolution, microstructures are confined near the slip planes [42,45]. The source of this athermal interface friction is tensile stresses in the region where atomic planes are missing. However, from the other side of the slip planes, extra planes producing dislocations provide considerable compressive stress concentrators, i.e., they promote the nucleation and stabilization of HPP as the new nucleation sites. The concentration of the HPP in Fig. 4(d) ( $\tilde{c} = 0.35$ ) is lower than Fig. 4(c) ( $\tilde{c} = 0.48$ ) due to the stress relaxation mechanism introduced by the slip systems. In other words, the plasticity plays two opposite roles: it provides dislocation pileups which are strong stress concentrators leading to the nucleation of the HPP regions; on the other hand, it relaxes the stresses formed during the evolution of dislocations on the slip systems. Depending on the deformation mechanisms, orientation of the grains, crystal lattices of the parent and product phases, and the loading conditions, the plasticity effects can be controlled [15,16].

The contour lines of the pressure and the shear stress evolutions are drawn in Fig. 6 and Fig. 7 for different microstructures presented in Fig. 4(a) and (b), including stationary solutions at the end. For the pressure distribution, the first distinguishable point is that there are both negative and positive pressures around the tip of pileups which can cause direct and reverse PT. In Fig. 6, there are negative (tensile) pressures in the most regions of the grain, due to the relatively high volume reductions during the PT, and a positive pressure in the LPP near the corners. At the beginning, the transformed regions are surrounded by high negative pressures (-7 ; however, at the stationary solutions, they aresurrounded by lower negative pressures (-3 GPa). On theother hand, in Fig. 7, the phase interface is close to the positive pressure at the beginning, and because of a considerable volume reduction in the HPP, they are embraced by negative pressures at the end. Also, in Fig. 6, the shear stress and pressure remain almost the same near the pileups since in Fig. 4(a), the loading of type-1 is applied, in contrast to Fig. 7 in which the shear stress concentration increases during the loading. While pressure is well below the phase equilibrium pressure and is even tensile, very large shear stresses contribute to the phase equilibrium condition at the phase interfaces.

The local thermodynamic phase equilibrium condition for any material point belonging to the sharp interface in elastoplastic material is X = 0, where X is the thermodynamic driving force for in-



**Fig. 5.** The effect of changes in the size of the sample on the number of dislocations, *n*. Loading scenario (type-1), boundary conditions, and the morphology of the HPP remain the same as presented in Fig. 2. The legend shows the scale factor for each sample.

terface motion. For neglected surface energy, X is the Eshelby driving force minus plastic work at the interface, see [46–48]. When also the elastic properties of both phases are the same, equation for X simplifies to  $X = \sigma : \varepsilon_t - \Delta G^{\theta}(\theta)$ . Then the local thermodynamic phase equilibrium condition for a material point that belongs to the sharp interface looks like

$$\sigma : \varepsilon_t = \Delta G^{\theta}(\theta) = 1.0 \, \text{GPa}. \tag{6}$$

Here,  $\sigma$ :  $\varepsilon_t$  is the transformation work (mechanical part of the driving force for the PT). The transformation work isolines for the stationary solution for several cases are plotted in the last row of Fig. 4. As one can see, the LPP-HPP interfaces are mostly coinciding with the  $\sigma$ :  $\varepsilon_t = 1.0$  GPa isolines, which is in agreement with the nanoscale PFA containing gradient energy [16,17]. One can surprisingly observe from Eq. (6) that the plastic strain does not contribute explicitly to the local phase equilibrium condition, but it is involved indirectly by changing the local stresses. Thus, neglecting the gradient energy in the current scale-free model for PT does not introduce an additional athermal resistance to the interface motion. In addition, the thermodynamic equilibrium conditions for the interfaces within the nanoscale and scale-free PFA are the same.

The evolution of the volume fraction of HPP,  $c \in [0, 1]$ , and the pressure averaged over the right and both grains are depicted in Fig. 8 for  $\varphi_1 = 89.7^{\circ}$ . For the case with excluded plasticity in

the right grain, Fig. 8(a), the average pressure over both grains decreases from 2 GPa to a value close to zero ( $\bar{P}=0.11$  GPa). A clear correlation can be recognized by seeing  $\tilde{c}$  and  $\bar{P}$  curves. The nucleation and growth of the HPP significantly reduce the pressure averaged over the entire sample due to a considerable reduction in the volume in the right grain during the PT. This happens because the volumetric transformation strain is compressive, and any increase in the volume fraction of the HPP leads to the volume reduction in the grain. Due to the shear stress relaxation in the right grain for the case with plasticity, Fig. 8(b), and consequently less HPP, the average pressure over both grains is not being reduced as drastic as in the previous case. Two different stages are clearly seen in Fig. 8: burst-like nucleation and growth, during which a major portion of the HPP appears and a drastic drop in pressure occurs, followed by a slow evolution toward the stationary solutions.

# 3.2. Phase transformation in a polycrystalline aggregate under compression and shear caused by dislocation pileups

For a further study of the present model, we implement it to a 200  $\times$  160 polycrystalline aggregate with 38 grains. The crystal orientation angles  $\varphi_1$  are shown inside each grain in Fig. 9(a). Two vertical edges are subjected to a displacement-periodic boundary condition, and the bottom edge of the sample is constrained from displacing in x and y directions. At the top edge, a prescribed normal stress,  $\sigma_n = 6.05$  GPa, and a low macroscopic shear strain rate,  $\dot{\gamma} = 0.004 \, \mathrm{s}^{-1}$ , are applied. The most active slip systems in each grain can be seen in Fig. 10, and the critical resolved shear stress on these contact surfaces is  $\tau_c = 0.3$  GPa. The arbitrarily determined location, quantity, and spacing of the active slip systems are due to the initial microstructure heterogeneities and internal stresses. Since grains are distributed by various sizes, orientations, and locations, there is a very heterogeneous distribution of the HPP, which is observed in Fig. 9(d) for four randomly chosen grains. The lowest averaged volume fraction of the HPP appears in the corner of grain #24, and the most transformed grains are #4 and #5 at the top middle of the sample. Moreover, reverse PT happens in some grains despite the monotonous shearing. In Fig. 9(b) and (c), a comparison between the pressure, shear, and volume fractions of the HPP and the corresponding variants averaged over the entire aggregates with 13 grains [29] and 38 grains are shown.

For the sample with 38 grains in Fig. 9(c), the averaged volume fraction of two variants are close to each other before  $\gamma \sim 0.15$ , however, by increasing  $\gamma$ ,  $\bar{c}_2$  becomes larger than  $\bar{c}_1$ . On the other hand, for the aggregate with 13 grains, the volume fraction of the variant 1 is always larger than variant 2. While in most grains both variants are activated, just one variant is mostly dominant in a

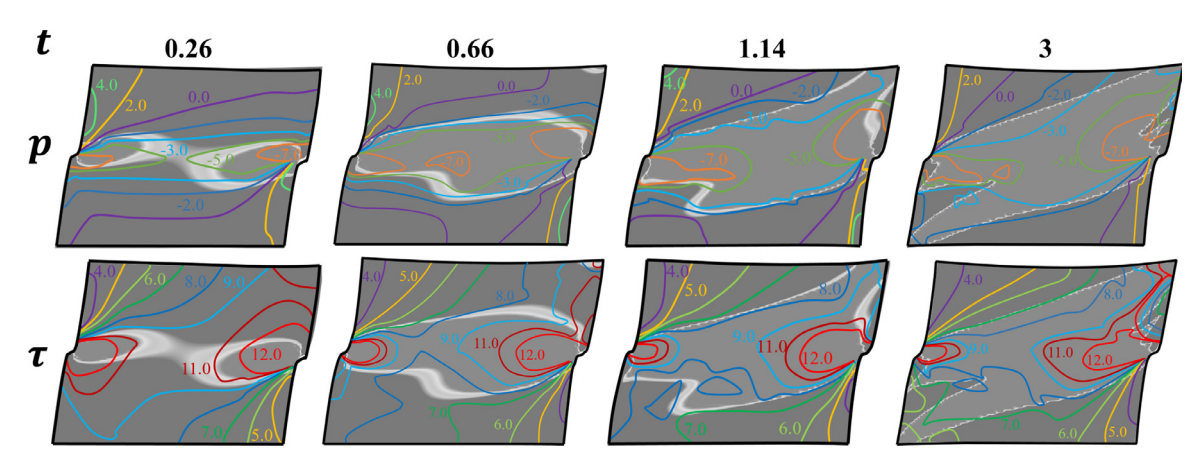


Fig. 6. Evolution of pressure and shear stress isolines in the transformed grain in Fig. 4(a). White regions and lines represent diffuse (finite-width) phase interfaces.

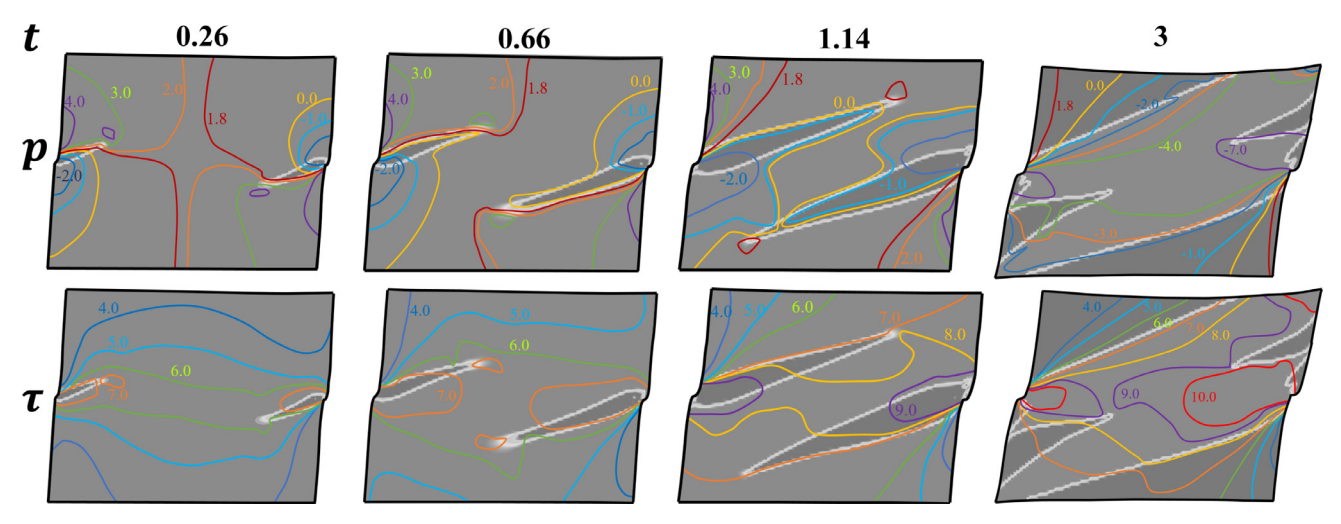
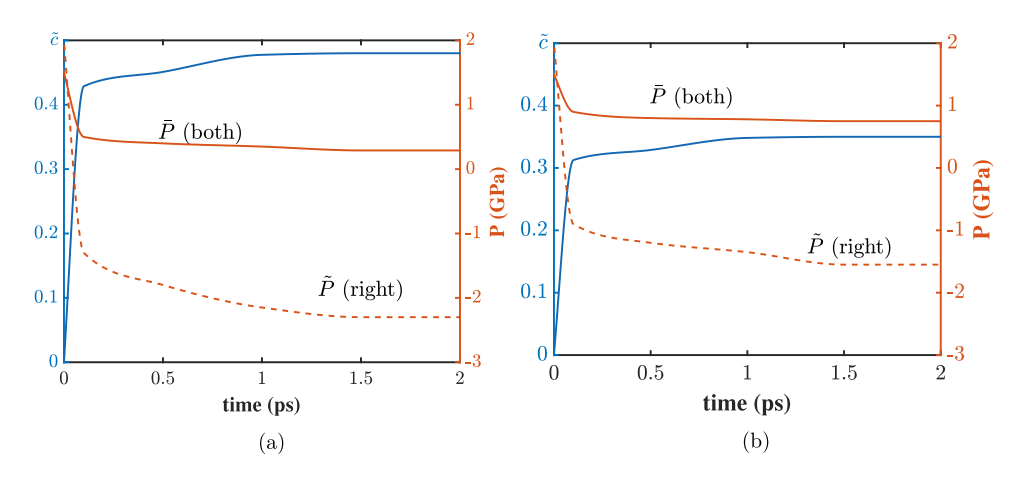


Fig. 7. Evolution of pressure and shear stress isolines in the transformed grain in Fig. 4(b).



**Fig. 8.** Evolution of the volume fraction of HPP, c, in the right grain, and the pressure averaged over the right grain and both grains for the cases (a) in Fig. 4(c), and (b) in Fig. 4(d), for  $\gamma = 0.2$ .

couple of them, which can be explained by the specific grain orientations (e.g., grain 26 in Fig. 10). For the sample with 38 grains, in Fig. 9(b),  $\bar{P}$  rises to ~ 5.0 GPa before the HPP is being experimentally detectable ( $\bar{c} \lesssim 0.05$ , see [13]), and after that, the averaged pressure reduces to ~ 1.8 GPa as a consequence of a significant reduction of the volume during the PT. Interestingly, the same trend can be seen for the aggregate with 13 gains. The averaged shear stress,  $\bar{\tau}$ , increases to ~ 2.9 GPa for 38 grains and 1.9 GPa for 13 grains because of the number of the dislocations (dislocation density) and back stresses from the dislocation pileups at grain boundaries. While our model for the single crystal corresponds to the perfect plasticity with  $\tau_c = 0.3$  GPa, the stochastic grain orientation and increasing energy of internal (back) stresses produce significant work hardening. A higher yield strength for the 38-grains aggregate than the value for the 13-grains one mimics the grainsize effect. Indeed, a larger number of grains in the samples of the same size results in a relatively smaller grain size and hinders the dislocation motion. However, this effect strongly depends on the prescribed strain, and we do not have sufficient data to quantify it in terms of the strain-dependent Hall-Petch equation.

Since the magnitude of the volumetric transformation strain of 0.1 is two times smaller than the shear transformation strain of 0.2, based on Fig. 9(b), the initial contribution of the pressure  $\bar{p}$  to the transformation work is significantly larger than the contribu-

tion of the shear stress  $\bar{\tau}$ . However, for  $\gamma \simeq 0.25$ , the shear stress effect becomes comparable, and with further straining, the shear stress contributes to a larger portion of the transformation work than the pressure, even more than a factor of 2 for 38 grains at  $\gamma = 0.33$ .

Kinetic curves for  $\bar{c}$  show that for 13 grains the phase transformation occurs faster than the case of 38 grains, despite the fact that the averaged pressure  $\bar{p}$  and the shear stress  $\bar{\tau}$ , and consequently, the transformation work are larger for 38 grains. Probably, with larger grains, (a) longer dislocation pileups can be accommodated within the grain producing stronger stress concentrators for nucleation, and (b) relatively a smaller grain-boundary area produces a smaller overall resistance to the phase-interface motion. However, surprisingly, for both samples the stationary (i.e., independent of shear) volume fraction of HPP,  $\bar{c}=0.7$ , exists for large shears and is independent of the number of grains. Fig. 9d confirms that while the entire HPP is in a stationary state, each martensitic variant in the entire sample is also practically in the stationary state, but the HPP and each martensitic variant reaches the stationary state in some grains.

The existence of stationary two-phase and multiphase solutions for the volume fraction of the strain-induced HPP is predicted and analyzed based on the microscale kinetic model [4,49] for the case when the minimum pressure for the direct strain-induced PT to

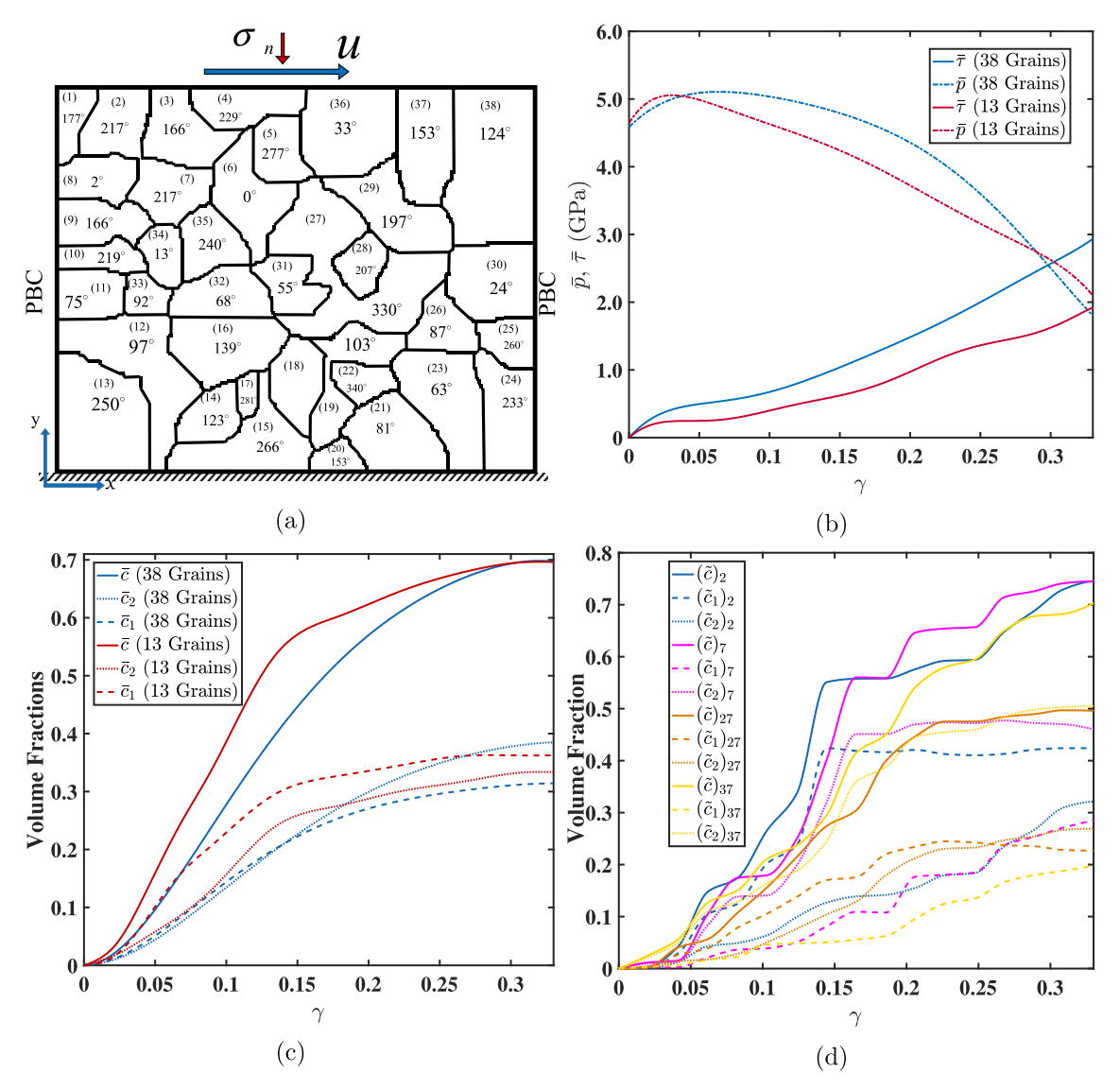


**Fig. 9.** (a) A schematic view of the polycrystalline aggregate under  $\sigma_n = 6.05$  GPa and  $\dot{\gamma} = 0.004 \, \text{s}^{-1}$ ; grain structures and their orientations presented by  $\varphi_1$  angle are shown in each grain along with the grain # in parentheses; (b) evolutions of the averaged pressure and shear for aggregates with 13 [29] and 38 grains, versus the macroscopic shear strain; (c) evolution of the overall volume fraction of the HPP for aggregates with 13 [29] and 38 grains, and (d) evolution of averaged volume fraction of the HPP,  $\tilde{c}$ , in several randomly-selected grains, and the corresponding martensitic variants,  $\tilde{c}_1$  and  $\tilde{c}_2$ , versus the prescribed shear strain.

the HPP is smaller than the maximum pressure for the reverse strain-induced PT to the LPP. This means that the effect of plastic strain on such a PT is very strong. Stationary states in [4,49] are uniquely determined by the applied pressure and they are independent of the process history in terms of pressure-plastic strain loading paths. There is a recent experimental confirmation of the kinetic equation from [4,49] for Zr [13], but a reverse PT did not occur in [13] and PT to the HPP is complete. Also, the existence of a stationary incompletely transformed solution and its loading history-independence are confirmed experimentally in [50]. The existence of the two-phase stationary solution also means that further shearing is pointless from the point of view of increasing the amount of HPP. This is one more illustration of the fact [4,5,8,49,51] that the plastic shear should be large enough but also optimal, thus, not as large as possible.

It can be seen from Fig. 10 that the HPP usually nucleates close to the extra atomic planes producing dislocations and also near the tip of the dislocation pileups in the adjoining grains. Kinetic curves for the volume fraction of the entire HPP and the martensitic vari-

ants in the individual grains (Fig. 9(d)) possess multiple plateaus and fast-growth stages. Plateaus correspond to the increasing the number of dislocations accommodating the increasing prescribed shear. When new dislocations join dislocation pileups and increase the local stress concentrations, the fast-growth stages occur, including coalescence of different HPP regions.

#### 3.3. Transformation-work based analysis

Local transformation work at interfaces. The stationary state of the microstructure and isolines of the equilibrium transformation work (see Eq. (6)) are drawn in Figs. 10 and 4 for various cases. Although there are some deviations between interfaces and the local equilibrium PT work contour lines Eq. (6) (mostly near the highstress concentrators, at slip surfaces, and around significant curvatures), they perfectly or closely coincide with each other in most regions of the various samples. This is more obvious in the bicrystal samples because there is a very small number of stress concentrations, i.e. pileups. This result has the following consequences:

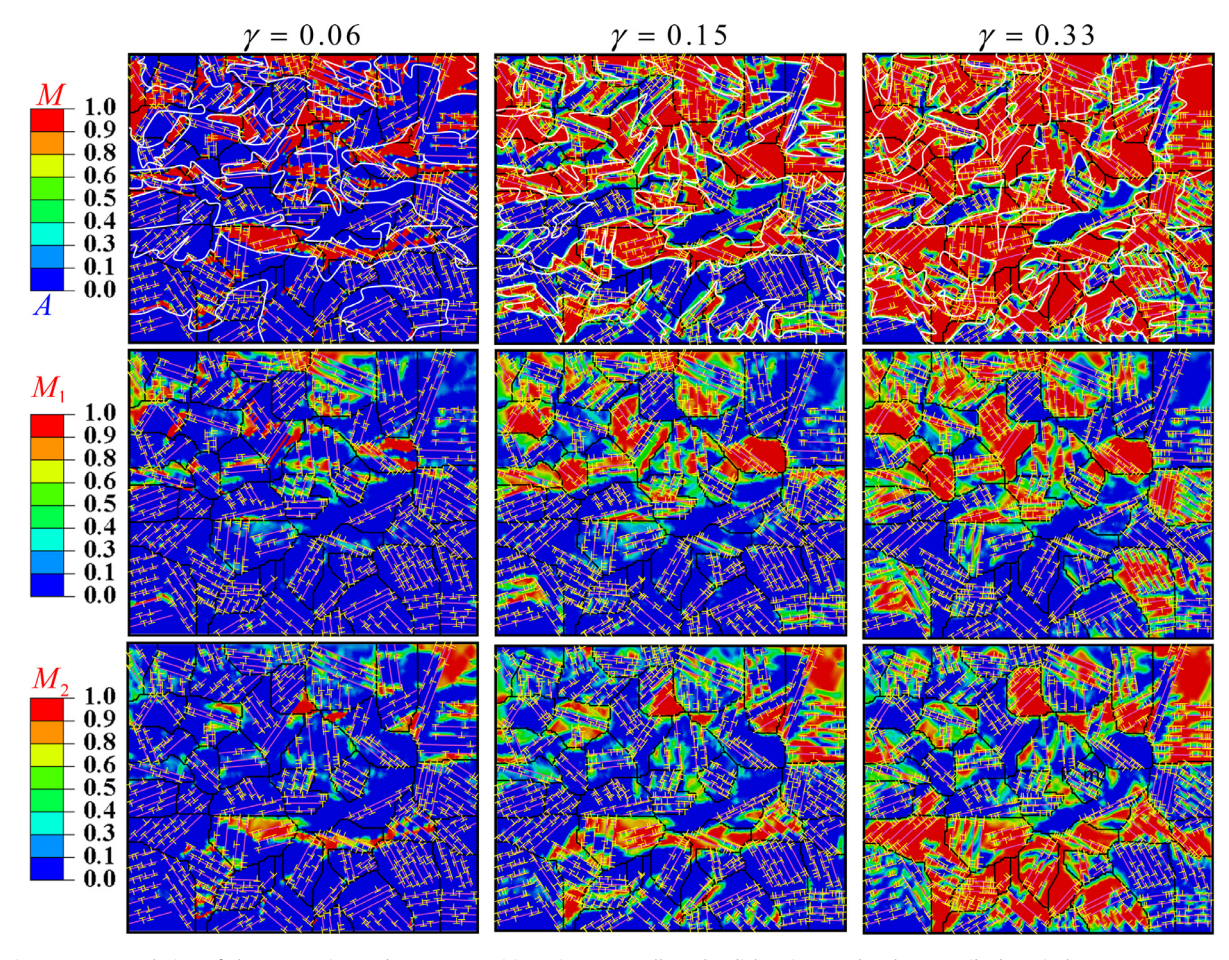


**Fig. 10.** Microstructure evolution of the martensite, and two martensitic variants as well as the dislocations under the prescribed vertical stress  $\sigma_n$  =6.05 GPa and  $\dot{\gamma}$  = 0.004 s<sup>-1</sup> at the top edge of the sample in Fig. 9.

(a) Due to the lack of the gradient term, theoretically, the PT in each point should occur independently of PT in the other points, when the peak stress at the stress-strain curve is reached [19-21], rather than at the phase equilibrium (Maxwell) stress described by Eq. (6). That is why fulfillment of the phase equilibrium conditions, Eq. (6), at interfaces means that, in a discretized form, our gradient-free model behaves like the traditional nanoscale phase field models with a gradient term [16,17,28]. While this is a topic for a separate study, we assume that the large gradient of the transformation strain within a diffuse interface containing one or few finite elements, produces large elastic stresses and energy within the interface (i.e., an interface energy), which plays the same part as the interface energy produced by the gradient energy term. Thus, while we do not penalize the gradient of the volume fraction of the HPP in the analytical equations, it is penalized in discrete equations due to the finite interface width and elastic energy. This assumption explains the fulfillment of Eq. (6) at stationary interfaces and the closeness of the results of the current scale-free model and nanoscale models [16,17,28].

(b) Note that in some sharp-interface based works [52,53] the total work  $\sigma$ : $\epsilon$  (i.e., the Eshelby driving force for the interface propagation) was utilized for elastoplastic materials, while in our papers [46–48,51] the phase equilibrium criterion (6) was derived. Current results support excluding plastic work from the phase equilibrium conditions, declared in [46–48,51].

(c) While plasticity does not explicitly contribute to (6), dislocations generate internal stresses, which significantly contribute to the total stresses in (6). If we separate internal stresses from

the external ones, the transformation work of the internal stresses can be moved to the right-hand side of (6). Then it represents an athermal resistance to the interface motion. This is evident in Figs. 10 and 4, where interfaces are arrested by the slip planes, namely by tensile stresses produced by the missing planes of dislocations. Thus, while athermal friction k is not explicitly introduced in the current examples, it appears in the solution due to the internal stresses of dislocations.

Transformation-work averaged over different regions. We assume that the interface width is relatively thin in comparison to the transformed region in the sample. With this assumption, the transformation work averaged over the entire volume is defined as follows:

$$\langle \sigma : \varepsilon_t \rangle_0 = \bar{c} \langle \sigma : \varepsilon_t \rangle_M + (1 - \bar{c}) \langle \sigma : \varepsilon_t \rangle_A, \tag{7}$$

in which  $\langle \ldots \rangle_M = \frac{1}{V_M} \int \ldots dV_M$ ,  $\langle \ldots \rangle_A = \frac{1}{V_A} \int \ldots dV_A$ , and  $\langle \ldots \rangle_0 = \frac{1}{V_0} \int \ldots dV_0$  indicate averaging over the HPP area, LPP area, and over the entire transformed sample, respectively. In addition to the actual solutions, we assume some artificial distribution of the transformation strain tensor in the LPP. In particular, for single-variant PT in a single crystal, we assume that  $\varepsilon_t = \varepsilon_{t1}$  is uniform and the same in HPP and LPP. Then Eq. (7) simplifies to

$$W_t^* := \langle \sigma \rangle_0 : \varepsilon_{t1} = (\bar{c} \langle \sigma \rangle_M + (1 - \bar{c}) \langle \sigma \rangle_A) : \varepsilon_{t1}, \tag{8}$$

which is identity because  $\langle \boldsymbol{\sigma} \rangle_0 = \bar{c} \langle \boldsymbol{\sigma} \rangle_M + (1 - \bar{c}) \langle \boldsymbol{\sigma} \rangle_A$ . Thus,  $W_t^*$  is some artificial transformation work produced by stresses averaged over the entire volume and the transformation strain in the HPP. We also introduce the actual transformation work per unit total

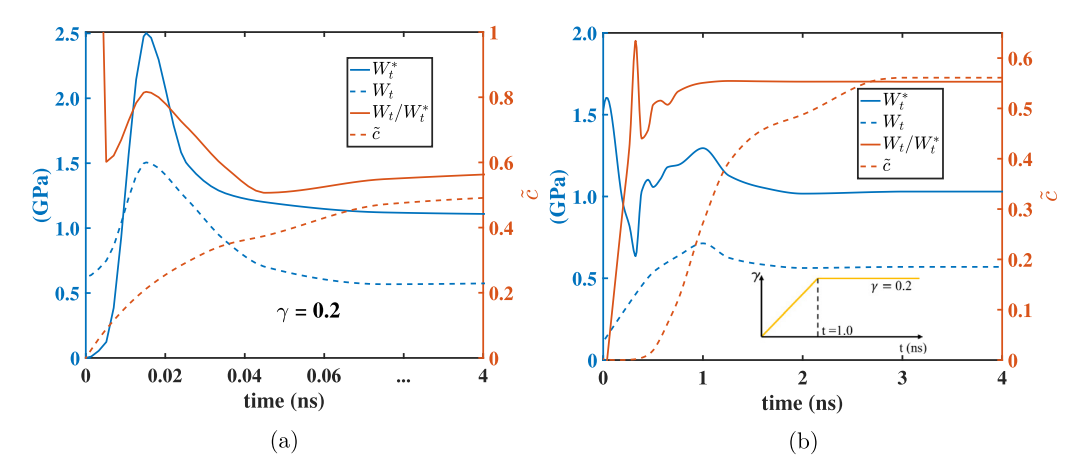


**Fig. 11.** Evolution of the volume fraction of HPP,  $\tilde{c}$ , in the right grain, the average transformation works  $W_t$  and  $W_t^*$  over the right grain, and their ratio for the cases (a) in Fig. 4(a) and (b) in Fig. 4(b).

**Table 1**Averaged transformation works defined by Eqs. (9) and (8) as well as the volume fraction of the HPP for different cases at the stationary state.

	$W_t(GPa)$	$W_t^*$ (GPa)	$W_t/W_t^*$	$ar{c}$
Fig. 4(a)	0.590	1.022	0.577	0.588
Fig. 4(b)	0.570	1.030	0.553	0.561
Fig. 4(c)	0.502	1.002	0.501	0.48
Fig. 4(d)	0.381	0.989	0.385	0.35
Fig. 10	0.696	1.097	0.634	0.7

volume,  $W_t$ , the actual transformation work per unit volume of the HPP,  $W_M$ , and the artificial transformation work per unit volume of the LPP,  $W_A$ ,

$$W_t := \langle \sigma : \varepsilon_t \rangle_M \bar{c} = \langle \sigma \rangle_M : \varepsilon_{t1} \bar{c}; \tag{9}$$

$$W_M := \langle \sigma : \varepsilon_t \rangle_M = \langle \sigma \rangle_M : \varepsilon_{t1};$$
  

$$W_A := \langle \sigma : \varepsilon_t \rangle_A = \langle \sigma \rangle_A : \varepsilon_{t1}$$
(10)

The values for  $W_t$ ,  $W_t^*$ ,  $W_t/W_t^*$ , and  $\bar{c}$  are tabulated in Table 1 to check out the averaged equilibrium transformational work condition in the stationary state. The ratio of  $W_t/W_t^*$  is approximately equal to  $\bar{c}$  for all cases, except for the case with small  $\bar{c}$  due to the plasticity introduced in the right grain of the bicrystal sample (Fig. 4(d)) and the polycrystalline aggregate (Fig. 10). The deviation for the mentioned cases are expected due to the comparable sizes of the interface width and the bulk HPP region, which is in contrast to our thin interface width assumption.

As a conclusion of analyzing Table 1, we can express

$$W_{M} = \langle \sigma \rangle_{M} : \varepsilon_{t1} \simeq W_{t}^{*} = \langle \sigma \rangle_{0} : \varepsilon_{t1} \simeq \Delta G \Longrightarrow \langle \sigma \rangle_{0} \simeq \langle \sigma \rangle_{M}.$$
(11)

Substituting Eq. (11) in Eq. (8) we also obtain

$$W_A := \langle \sigma \rangle_A : \varepsilon_{t1} \simeq \langle \sigma \rangle_M : \varepsilon_{t1}; \implies \langle \sigma \rangle_A \simeq \langle \sigma \rangle_M \simeq \langle \sigma \rangle_0.$$
(12)

Obtaining the approximate equality of the stresses averaged over the HPP, LPP, and the entire sample was the reason for introducing artificial transformation strain in the LPP.

In Fig. 11(a) and (b), the evolution of the averaged transformation works  $W_t$  and  $W_t^*$ , their ratio, and the volume fraction of the HPP over the right grain are presented for the results shown in Fig. 4(a) and (b). As mentioned previously, the only difference between these two cases is in the loading scenario (the macroscopic

shear strain of 0.2 is applied instantaneously in Fig. 11(a)). As presented,  $W_t/W_t^*$  in Fig. 11(a) is not close to the volume fraction of the HPP at the very beginning due to a small transformed region and relatively large interfaces. As expected, especially in Fig. 11(b),  $W_t/W_t^*$  increases until the nucleation starts and then it drops and converges to  $\tilde{c}$  at the stationary state. Due to the different loading scenario, in Fig. 11(a),  $W_t/W_t^*$  is initially large and then drops, which is resulted from a constant  $\gamma$ .

For the polycrystalline aggregate with two variants, we artificially assume that the transformation strain over the entire sample  $(\varepsilon_t)$  is the same for both LPP and HPP, which is described as

$$\boldsymbol{\varepsilon_t} = \bar{c_1}\bar{\boldsymbol{\varepsilon}_{t1}} + \bar{c_2}\bar{\boldsymbol{\varepsilon}_{t2}} . \tag{13}$$

Here  $\bar{\varepsilon}_{t1}$  and  $\bar{\varepsilon}_{t1}$  are the transformation strains for each variant averaged over the entire polycrystalline aggregate with N grains, which are defined as

$$\bar{\boldsymbol{\varepsilon}}_{ti} := \frac{\sum_{j=1}^{N} V_j \tilde{c}_i^j \boldsymbol{\varepsilon}_{ti}^j}{\sum_{i=1}^{N} V_i \tilde{c}_i^j}; \quad i = 1 \& 2, \tag{14}$$

where  $V_j$  is the volume of the jth grain. By doing the same calculations as in Eqs. (7)–(12), and using the results in Table 1 along with the definition in Eq. (13), the same conclusions as Eqs. (11), (12) can be also achieved for the polycrystalline aggregate. However, when we consider each grain separately and use the local transformation strain in a grain, the transformation work averaged over the volume of each grain is not generally equal to  $\Delta G$ , see Fig. 12. Different definitions of the transformation work generally give the different results in Fig. 12. The reason for the deviations is that for the entire volume of a bicrystal and polycrystalline, the macroscopically homogeneous boundary conditions for stresses and strains, are prescribed; however, this is not true for each grain.

The obtained local Eq. (6) and averaged Eq. (11) phase equilibrium criteria which approximate the equality of stresses averaged over HPP, LPP, and the entire sample, are very important for the development of the coarse-grained theory of the interaction between phase transformation and plasticity for the entire polycrystalline aggregate. Also, the kinetic curves Fig. 9(b)–(d) are crucial for the development of a more accurate microscale kinetic equation for the plastic strain induced phase transformation than those suggested in [4,49]. This kinetic equation is currently used within a macroscale computational model for studying the behavior of a sample under compression and compression-torsion in traditional and rotational diamond anvils [54–57].

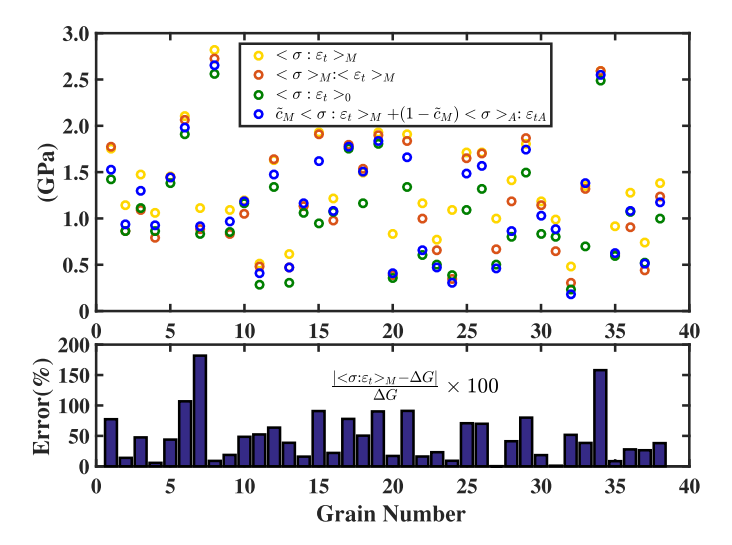


**Fig. 12.** Transformation works averaged over each grain of the polycrystalline aggregate from Fig. 9(a) based on different definitions (top) and deviations of the  $\langle \sigma \colon \mathcal{E}_t \rangle_M$  from  $\Delta G$  (bottom).

#### 4. Concluding remarks

In this work, a scale-independent model for the interactions between the evolution of discrete shear bands and multivariant martensitic PTs is advanced and applied for studying plastic flow and PT in a bicrystal and polycrystalline aggregate under high pressure and shear. The model includes a scale-free phase field theory for multivariant martensitic PTs, which does not possess a gradient energy term, and consequently, characteristic size. Still, the solution is practically mesh independent because the material instability localizes within the FE-size width of the interface between LPP and HPP. This interface is usually small in comparison to bulk LPP and HPP, exhibiting a stable and well-posed behavior [19]. Also, while we neglect the gradient of the order parameter (i.e., the volume fraction of the HPP) in the analytical equations, it is penalized in the discrete equations due to the finite numerical interface width and elastic energy. Indeed, a large gradient of the volume fraction of the HPP and consequently, the transformation strain within a diffuse interface produces large elastic stresses and energy within an interface (i.e., interface energy), which is similar to the interface energy produced by the gradient energy term. Without the gradient energy term, PT in each material point occurs independently of PT in other points when the peak stress at the stress-strain curve is reached [19-21]. With an "effective" gradient energy, a phase interface is at a thermodynamic equilibrium when Eq. (6) is met for the interface points, like in traditional nanoscale PFA [16,17,28] with a gradient term.

Plastic flow in our approach is modelled through continuous sliding along the prescribed discrete slip planes and directions. This sliding may represent dislocation pileups [30,31], thin twins [31], shear cracks [33], or macroscopic shear bands [32]. The key point is that such a discretized plasticity reproduces strong stress concentrators at the tip of these defects and in the places of large gradients of sliding displacements, similar to the pileup of discrete dislocations [16,17,28]. These plastic-strain-induced stress concentrators serve as nucleation cites for strain-induced PTs, like in a nanoscale PFA [16,17,28]. The advantage of the scale-free PFA is that it is not limited to the submicron samples, like nanoscale PFA, but can be applied to an arbitrary sample size exceeding tens of nm up to km (for geophysical applications). Scaleindependency of the suggested model is also proved by treating geometrically similar samples and varying their size by three orders of magnitude. At the same time, our scale-free approach reproduces the stress field of a single dislocation and the solutions for a coupled evolution of dislocations and HPP in a nanoscale PFA [16,17,28], which is more sophisticated and computationally expensive.

In all problems, periodic boundary conditions for displacements at the lateral sides of samples are applied, along with normal compressive stresses and shear displacement at the upper surface with a fixed lower surface. For a bicrystal, dislocation pileup produces barrierless nucleation and growth of the HPP, including a coalescence stage. Dislocation pileup reduces the PT pressure from 14.7 GPa under hydrostatic loading to 0.07 GPa under shear. This confirms conceptually the ability of dislocation pileup to describe experiments in which plastic shear reduced the PT pressure by one order of magnitude [7,9-12] and even two orders of magnitude [14] in comparison to the hydrostatic loading. Note that the PT pressure under shear is also significantly below the phase equilibrium pressure under the hydrostatic conditions, 10 GPa, like in some experiments [7,13]. However, dislocations not only promote PT; in some cases, they also suppress PT by relaxing internal stresses and by producing an athermal threshold to the dislocation motion. While compressive stresses due to extra planes, which produce dislocations, promote PT (in addition to the stress concentrator at the tip of dislocation pileup), tensile stresses due to missing planes confine the PT. Thus, in some cases, the phase interface coincides with the slip plane.

Transformation kinetics versus shear strain for each martensitic variant and the total volume fraction of the HPP, in each grain and in the entire polycrystal, are determined for two 2D polycrystalline aggregates consisting of 13 and 38 grains. The results are not significantly different for both aggregates; in particular, the stationary (i.e., independent of shear) volume fraction of the HPP for large macroscopic shear values, 0.7, is the same for both aggregates. This observation reflects the fact that such a relatively small number of grains provides a representative transformational behavior of the polycrystal. At the same time, strain hardening is higher for the aggregate with 38 grains due to the grain-size effect.

The existence of the incomplete transformation, i.e., the stationary volume fraction of HPP independent of the applied shear, was also predicted and analyzed based on the microscale kinetic model [4,49] for the case when the effect of plastic strain on the PT is very strong. Stationary states in [4,49] are uniquely determined by the applied pressure and they are independent of the process history in terms of pressure-plastic strain loading paths. The existence of a stationary incompletely transformed solution and its loading history independence was confirmed experimentally in [50]. Such a stationary state also demonstrates that the plastic shear should be optimal rather than just being large, as it was assumed previously

Interestingly, even for complex systems such as the polycrystalline aggregate with numerous dislocation bands, the simplest local phase equilibrium condition Eq. (6) is satisfied for almost all stationary interfaces. Thus, this equation can be treated as a general result, which explains the closeness of the solutions for the current scale-free model and nanoscale models [16,17,28] for a bicrystal. The transformation-based work criterion, which does not include plastic work, supports our previously derived criterion for sharp interfaces [46–48,51] and confronts the total-work (i.e., based on the Eshelby driving force) criterion in [52,53].

It is shown that a similar global phase equilibrium condition in terms of the stresses averaged over the entire polycrystalline sample, or HPP is met. The global phase equilibrium conditions, however, are not fulfilled for each grain or for non-stationary solutions. The obtained approximate equality of the stresses averaged over the entire polycrystal and HPP and LPP, for such complex fields and large numbers of grains, is also very nontrivial and an important result.

While plasticity does not explicitly contribute to the local and global phase equilibrium condition, dislocations generate internal stresses, which significantly change the total stresses, and thus contribute to the phase equilibrium conditions implicitly. In fact, they represent an athermal resistance to the interface motion due to the presence of dislocations.

The major contribution to the averaged transformation work comes from pressure at the initial stage of PT and from shear stress at the later stage. This happens because pressure drops due to the volume reduction and shear stress growth due to the strain hardening caused by the back stresses. This demonstrates that shear (more generally, deviatoric) stresses should be incorporated in the microscale kinetics for the strain-induced PTs [4,49]. The acquired overall kinetics, local and global phase equilibrium conditions, and equality of the stresses averaged over phases and entire polycrystal will be utilized for the further advancement of kinetic equations in [4,49], especially for the case when pressure (or stress) induced PTs occur simultaneously with the strain-induced PTs. Such kinetics equations are important for the modeling of the sample behavior in traditional and rotational diamond anvils [54-57], during high-pressure torsion, ball milling, friction, and other deformationtransformation processes.

#### **Declaration of Competing Interest**

Declaration of Interest Statement As corresponding author, Valery Levitas, hereby confirm on behalf of all authors that: (1) the authors have no affiliation with any organization with a direct or indirect financial interest in the subject matter discussed in the manuscript. (2) The authors have obtained the necessary authority for publication. (3) The paper does not contain material which has been published previously, by the current authors or by others, of which the source is not explicitly cited in the paper. Upon acceptance of an article by the journal, the author(s) will be asked to transfer the copyright of the article to the publisher. This transfer will ensure the widest possible dissemination of information.

# Acknowledgments

Support from NSF (CMMI-1943710 and MMN-1904830), ARO (W911NF-17-1-0225), ONR (N00014-16-1-2079), and the ISU (Vance Coffman Faculty Chair Professorship) are gratefully acknowledged. The simulations were performed at XSEDE, allocation TG-MSS140033.

#### Supplementary material

Supplementary material associated with this article can be found, in the online version, at doi:10.1016/j.actamat.2020.06.059.

#### References

- G.B. Olson, Computational design of hierarchically structured materials, Science 277 (5330) (1997) 1237–1242.
   P. Bridgman, Effects of high shearing stress combined with high hydrostatic
- pressure, Phys. Rev. 48 (10) (1935) 825.

  [3] V.I. Levitas, Continuum mechanical fundamentals of mechanochemistry, High
- [3] V.I. Levitas, Continuum mechanical fundamentals of mechanochemistry, High Press. Surf. Sci. Eng. 3 (2004) 159–292.
- [4] V.I. Levitas, High-pressure mechanochemistry: conceptual multiscale theory and interpretation of experiments, Phys. Rev. B 70 (18) (2004) 184118.
- [5] V.I. Levitas, Y. Ma, J. Hashemi, M. Holtz, N. Guven, Strain-induced disorder, phase transformations, and transformation-induced plasticity in hexagonal boron nitride under compression and shear in a rotational diamond anvil cell: in situ x-ray diffraction study and modeling, J. Chem. Phys. 125 (4) (2006) 044507.
- [6] V.I. Levitas, Y. Ma, E. Selvi, J. Wu, J.A. Patten, High-density amorphous phase of silicon carbide obtained under large plastic shear and high pressure, Phys. Rev. B 85 (5) (2012) 054114.
- [7] V.D. Blank, E.I. Estrin, Phase Transitions in Solids Under High Pressure, CRC Press, 2013.

- [8] V.I. Levitas, High-pressure phase transformations under severe plastic deformation by torsion in rotational anyils. Mater. Trans. 60 (7) (2019) 1294–1301.
- [9] V.I. Levitas, L.K. Shvedov, Low-pressure phase transformation from rhombohedral to cubic BN: experiment and theory. Phys. Rev. B 65 (10) (2002) 104109
- dral to cubic BN: experiment and theory, Phys. Rev. B 65 (10) (2002) 104109. [10] C. Ji, V.I. Levitas, H. Zhu, J. Chaudhuri, A. Marathe, Y. Ma, Shear-induced phase transition of nanocrystalline hexagonal boron nitride to wurtzitic structure at room temperature and lower pressure, Proc. Natl. Acad. Sci. 109 (47) (2012) 19108–19112.
- [11] M. Pérez-Prado, A. Zhilyaev, First experimental observation of shear induced hcp to bcc transformation in pure zr, Phys. Rev. Lett. 102 (17) (2009) 175504.
- [12] B. Srinivasarao, A. Zhilyaev, M. Perez-Prado, Orientation dependency of the alpha to omega plus beta transformation in commercially pure zirconium by high-pressure torsion, Scr. Mater. 65 (3) (2011) 241–244.
- [13] K. Pandey, V.I. Levitas, In situ quantitative study of plastic strain-induced phase transformations under high pressure: example for ultra-pure zr, Acta Mater. (2020), doi:10.1016/j.actamat.2020.06.015.
- [14] Y. Gao, Y. Ma, Q. An, V. Levitas, Y. Zhang, B. Feng, J. Chaudhuri, W.A. Goddard III, Shear driven formation of nano-diamonds at sub-gigapascals and 300 k, Carbon N Y 146 (2019) 364–368.
- [15] V.I. Levitas, M. Javanbakht, Phase transformations in nanograin materials under high pressure and plastic shear: nanoscale mechanisms, Nanoscale 6 (1) (2014) 162–166.
- [16] M. Javanbakht, V.I. Levitas, Phase field simulations of plastic strain-induced phase transformations under high pressure and large shear, Phys. Rev. B 94 (21) (2016) 214104.
- [17] M. Javanbakht, V.I. Levitas, Nanoscale mechanisms for high-pressure mechanochemistry: a phase field study, J. Mater. Sci. 53 (19) (2018) 13343–13363.
- [18] I. Steinbach, M. Apel, Multi phase field model for solid state transformation with elastic strain, Physica D 217 (2) (2006) 153–160.
- [19] S.E. Esfahani, I. Ghamarian, V.I. Levitas, P.C. Collins, Microscale phase field modeling of the martensitic transformation during cyclic loading of niti single crystal, Int. J. Solids Struct. 146 (2018) 80–96.
- [20] A. Idesman, V. Levitas, D. Preston, J.-Y. Cho, Finite element simulations of martensitic phase transitions and microstructures based on a strain softening model, J. Mech. Phys. Solids 53 (3) (2005) 495–523.
- [21] V.I. Levitas, A.V. Idesman, D.L. Preston, Microscale simulation of martensitic microstructure evolution, Phys. Rev. Lett. 93 (10) (2004) 105701.
- [22] D.C. Lagoudas, Shape Memory Alloys: Modeling and Engineering Applications, Springer, 2008.
- [23] C. Lexcellent, Shape-memory Alloys Handbook, John Wiley & Sons, 2013.
- [24] See supplemental material at url will be inserted by publisher– for the description of the scal-free model for martensitic pt and material parameters.
- [25] Y.U. Wang, Y. Jin, A. Cuitino, A. Khachaturyan, Nanoscale phase field microelasticity theory of dislocations: model and 3d simulations, Acta Mater. 49 (10) (2001) 1847–1857.
- [26] Y. Jin, A. Khachaturyan, Phase field microelasticity theory of dislocation dynamics in a polycrystal: model and three-dimensional simulations, Philos. Mag. Lett. 81 (9) (2001) 607-616.
- [27] V.I. Levitas, M. Javanbakht, Interaction between phase transformations and dislocations at the nanoscale. Part 1. General phase field approach, J. Mech. Phys. Solids 82 (2015) 287–319.
- [28] M. Javanbakht, V.I. Levitas, Interaction between phase transformations and dislocations at the nanoscale. Part 2: phase field simulation examples, J. Mech. Phys. Solids 82 (2015) 164–185.
- [29] V.I. Levitas, S.E. Esfahani, I. Ghamarian, Scale-free modeling of coupled evolution of discrete dislocation bands and multivariant martensitic microstructure, Phys. Rev. Lett. 121 (20) (2018) 205701.
- [30] J.P. Hirth, J. Lothe, T. Mura, Theory of dislocations, 1983.
- [31] V. Boyko, R. Garber, A. Kossevich, Reversible Crystal Plasticity, Springer Science & Business Media, 1997.
- [32] R.J. Asaro, Crystal plasticity, J. Appl. Mech. 50(4b) (1983) 921-934.
- [33] J. Rice, H. Leibowitz, in: Fracture: An Advanced Treatise, 11, Academic Press, New York, NY, 1968, pp. 214–223.
- [34] V. Abaqus, in: 6.14 Documentation, 651, Dassault Systemes Simulia Corporation, 2014, pp. 6–12.
- [35] M.A. Groeber, M.A. Jackson, Dream. 3d: a digital representation environment for the analysis of microstructure in 3d, Integr. Mater. Manuf. Innov. 3 (1) (2014) 5.
- [36] F. Bachmann, R. Hielscher, H. Schaeben, Texture analysis with mtex-free and open source software toolbox, in: Solid State Phenomena, 160, Trans Tech Publ, 2010, pp. 63–68.
- [37] H. Bunge, Some applications of the taylor theory of polycrystal plasticity, Krist. Tech. 5 (1) (1970) 145–175.
- [38] P. Wriggers, Computational Contact Mechanics, Springer-Verlag-Berlin, 2006.
- [39] V. Levitas, A. Idesman, E. Stein, Finite element simulation of martensitic phase transitions in elastoplastic materials, Int. J. Solids Struct. 35 (9–10) (1998) 855–887.
- [40] A.V. Idesman, V.I. Levitas, E. Stein, Structural changes in elastoplastic material: a unified finite-element approach to phase transformation, twinning and fracture, Int. J. Plast. 16 (7–8) (2000) 893–949.
- [41] O. Kolednik, W. Ochensberger, J. Predan, F. Fischer, Driving forces on dislocations – an analytical and finite element study, Int. J. Solids Struct. 190 (2020) 181–198.
- [42] V.I. Levitas, M. Javanbakht, Advanced phase-field approach to dislocation evolution, Phys. Rev. B 86 (14) (2012) 140101.

- [43] M.J. Serenelli, M.A. Bertinetti, J.W. Signorelli, Investigation of the dislocation slip assumption on formability of bcc sheet metals, Int. J. Mech. Sci. 52 (12) (2010) 1723–1734.
- [44] S. Li, A.A. Gazder, I.J. Beyerlein, C.H. Davies, E.V. Pereloma, Microstructure and texture evolution during equal channel angular extrusion of interstitial-free steel: effects of die angle and processing route, Acta Mater 55 (3) (2007) 1017–1032.
- [45] V.I. Levitas, M. Javanbakht, Phase field approach to interaction of phase transformation and dislocation evolution, Appl. Phys. Lett. 102 (25) (2013) 251904.
- [46] V.I. Levitas, Structural changes without stable intermediate state in inelastic material. part ii. applications to displacive and diffusional–displacive phase transformations, strain-induced chemical reactions and ductile fracture, Int. J. Plast. 16 (7–8) (2000) 851–892.
- [47] V.I. Levitas, Phase transitions in elastoplastic materials: continuum thermomechanical theory and examples of controlpart i, J. Mech. Phys. Solids 45 (6) (1997) 923–947.
- [48] V.I. Levitas, Thermomechanical theory of martensitic phase transformations in inelastic materials, Int. J. Solids Struct. 35 (9–10) (1998) 889–940.
- [49] V.I. Levitas, O.M. Zarechnyy, Kinetics of strain-induced structural changes under high pressure, J. Phys. Chem. B 110 (32) (2006) 16035–16046.
- [50] B.B. Straumal, A.R. Kilmametov, Y. Ivanisenko, A.A. Mazilkin, O.A. Kogtenkova, L. Kurmanaeva, A. Korneva, P. Zięba, B. Baretzky, Phase transitions induced by severe plastic deformation: steady-state and equifinality: paper presented at arXiv international conference on electron microscopy, 15–18 september 2014, cracow, poland, Int. J. Mater. Res. 106 (7) (2015) 657–664.

- [51] V.I. Levitas, Critical thought experiment to choose the driving force for interface propagation in inelastic materials, Int. J. Plast. 18 (11) (2002) 1499–1525.
- [52] M. Cherkaoui, M. Berveiller, Moving inelastic discontinuities and applications to martensitic phase transition, Arch. Appl. Mech. 70 (1–3) (2000) 159–181.
- [53] F. Fischer, G. Reisner, A criterion for the martensitic transformation of a microregion in an elastic-plastic material, Acta Mater. 46 (6) (1998) 2095–2102.
- [54] V.I. Levitas, O.M. Zarechnyy, Modeling and simulation of strain-induced phase transformations under compression and torsion in a rotational diamond anvil cell, Phys. Rev. B 82 (17) (2010) 174124.
- [55] B. Feng, V.I. Levitas, Effects of gasket on coupled plastic flow and strain-in-duced phase transformations under high pressure and large torsion in a rotational diamond anvil cell, J. Appl. Phys. 119 (1) (2016) 015902.
- [56] B. Feng, V.I. Levitas, Coupled elastoplasticity and plastic strain-induced phase transformation under high pressure and large strains: formulation and application to bn sample compressed in a diamond anvil cell, Int. J. Plast. 96 (2017) 156–181.
- [57] B. Feng, V.I. Levitas, W. Li, Fem modeling of plastic flow and strain-induced phase transformation in bn under high pressure and large shear in a rotational diamond anvil cell, Int. J. Plast. 113 (2019) 236–254.